Green Chemistry

PAPER

View Article Online
View Journal | View Issue

Check for updates

Cite this: *Green Chem.*, 2025, **27**, 660

Macromolecular electrolyte engineering for tuning Zn-ion solvation chemistry and boosting H^+ storage toward stable aqueous zinc-organic batteries†

Linqi Cheng,‡[a,b] Mengfan Li,‡[b] Xupeng Zhang,‡[b] Wanting Wang,[a] Lina Zhao*[a,c] and Heng-Guo Wang *[b]

Aqueous zinc-organic batteries (AZOBs) have attracted attention because they have the advantages of both organic batteries and aqueous zinc-ion batteries. Nevertheless, the hydrogen evolution reaction and the unrestrained growth of Zn dendrites still limit the further development of AZOBs. In this work, we demonstrate that the macromolecular electrolyte engineering using porphyrin derivatives with different peripheral substituents could not only restrain the solvation sheath of Zn^{2+} and inhibit the parasitic reactions but also boost H^+ storage for AZOBs. Among various porphyrin derivatives, the tetraphenylporphyrin tetrasulfonic acid (TPPS) additive has the ability to facilitate the formation of a Zn-porphyrin complex to promote uniform Zn^{2+} deposition, resulting in superior Zn symmetric cells with longer cycling stability over 900 h and smaller overpotential of 35.3 mV. Furthermore, the full cell and pouch-type cell with quinone-fused aza-phenazine (QAP) cathode also exhibit impressive electrochemical performance. Even at different bending angles, the change in specific capacities of pouch-type cells is negligible. These findings furnish an advanced concept for the application of porphyrin derivatives as an additive for the further development of AZOBs.

Received 11th October 2024,
Accepted 29th November 2024

DOI: 10.1039/d4gc05107f

rsc.li/greenchem

Published on 17 December 2024. Downloaded on 25/11/2025 6:45:18 AM.

Introduction

At present, aqueous zinc-ion batteries (AZIBs) are experiencing explosive development owing to their easy and safe operation conditions, abundant reserves, low cost and high theoretical capacity.[1–8] However, their large-scale commercial application is greatly hindered by insurmountable obstacles.[9,10] Relying heavily on inorganic electrode materials (IEMs) as cathodes will lead to soaring prices and environmental pollution similar to lithium-ion batteries. On the contrary, aqueous zinc-organic batteries (AZOBs) stand out because they utilize the advantages of organic electrode materials (OEMs), such as lower carbon footprints, abundant biomass resources, and excellent structural designability.[11–14] In addition, the redox reaction of OEMs is achieved through the rearrangement of chemical bonds rather than the insertion/extraction of the large-size divalent Zn^{2+} (often hydrated), thus avoiding the structure collapse that often happens in IEMs.[15–18] Interestingly, the aqueous electrolyte could also reduce the dissolution of OEMs caused by the organic electrolyte to a certain extent so that the conjugated small molecules can be directly used in AZOBs, thus avoiding the cost issues caused by the polymerization or composite.[19–22] Despite these unique advantages, there are still some obstacles for the practical use of AZOBs. Like AZIBs, the arbitrary growth of Zn dendrites and the uncontrolled hydrogen evolution reaction (HER) on the anode side can reduce the reversibility of Zn plating/stripping and ultimately lead to cell failure.[23–26]

To address these issues, various strategies have been developed, including electrolyte engineering, interface optimization and anode regulation.[27,28] Among these strategies, electrolyte engineering has attracted much attention due to its simplicity and ability to effectively re-invent the existing electrolyte systems.[29–33] Particularly, macrocyclic molecules and typically non-consumable electrolyte additives have been explored to optimize the electrode/electrolyte interface against electrolyte decomposition and dendrite growth. The macrocyclic confinement effect (such as crown ethers and cyclodextrins) can effec-

[a]*Key Laboratory of Preparation and Applications of Environment Friendly Materials, Ministry of Education, Jilin Normal University, Changchun 130103, P. R. China. E-mail: zhaolina1975@jlnu.edu.cn*
[b]*Key Laboratory of Polyoxometalate and Reticular Material Chemistry of Ministry of Education, Faculty of Chemistry, Northeast Normal University, Changchun 130024, P. R. China. E-mail: wanghengguo@cust.edu.cn*
[c]*College of Chemistry, Jilin Normal University, Siping, 136000, P. R. China*
†Electronic supplementary information (ESI) available. See DOI: **https://doi.org/10.1039/d4gc05107f**
‡These authors contributed equally to this work.

This journal is © The Royal Society of Chemistry 2025

Published on 17 December 2024. Downloaded on 25/11/2025 6:45:18 AM.

tively break the Zn^{2+} solvation sheath and regulate the inner Helmholtz plane (IHP) structure.[34–37] Furthermore, their hydrophilic outer surface and hydrophobic central cavity can regulate oriented Zn^{2+} deposition and suppress the water-induced side reactions. In this context, it is highly desired to develop macromolecular additives with a strong electrostatic shielding effect (Table S1†). Porphyrin and its derivatives are well known as typical macromolecular heterocyclic compounds. Firstly, they exist widely in organisms and are inexpensive and readily available natural materials. Secondly, they show many fascinating features of adaptability, benignity to the environment, easy degradation and naturally abundant elements (such as C, H, O, N). Thirdly, they possess the well-known structural designability of the central cavity and peripheral substituents, which is conducive to the modification of the electrolyte.[38–40] Especially, the central cavity possesses a strong binding effect with metal ions; the peripheral substituents could also introduce hydrophilic characteristics, which could endow them with a strong electrostatic shielding effect and de-solvation ability. Meanwhile, a highly conjugated π-electron system and carrier mobility could induce lower interfacial impedance and uniform surface current distributions. Therefore, the intensive exploration of porphyrin and its derivatives to tune Zn-ion solvation chemistry is very necessary. However, no examples of macromolecular electrolyte engineering for AZOBs have been reported so far.

Herein, we demonstrate the macromolecular electrolyte engineering to break the Zn^{2+} solvation sheath and inhibit the parasitic reactions enabled by porphyrin derivatives, and for the first time, extend its application in AZOBs. Moreover, the effect of different peripheral substituents (–SO_3H, –COOH, –NH_2 and –F) on tuning Zn-ion solvation chemistry is comparatively investigated and screened. Interestingly, their central cavity shows strong binding ability with Zn^{2+}, which not only breaks the Zn^{2+} solvation sheath but also facilitates the Zn^{2+} transportation. Encouragingly, tetraphenylporphyrin tetrasulfonic acid (TPPS) with peripheral –SO_3H first undergoes the H^+ dissociation; meanwhile, the generated sulfonate shows stronger binding ability with zinc ions, further guiding more uniform Zn deposition. Therefore, the Zn‖Zn symmetric cells with the optimum electrolyte (2 M $ZnSO_4$ + TPPS-4) display a long cycling lifetime of over 900 h at 0.5 mA cm^{-2}. By coupling with quinone-fused aza-phenazine (QAP) as the model cathode material, the full cell and the pouch-type cell demonstrate improved electrochemical performance. Furthermore, the dissociation of H^+ from the TPPS additive could boost the H^+ storage of the cathode material, thus achieving the reversible Zn^{2+}/H^+ synergistic storage mechanism of QAP.

Results and discussion

Fig. 1a shows the molecular structure of different porphyrin additives, which reveals that the central cavity containing nitrogen functional groups is highly polar and the four peripheral substituents (–SO_3H, –COOH, –NH_2 and –F) give them the hydrophilic/hydrophobic outer surface, and this dual

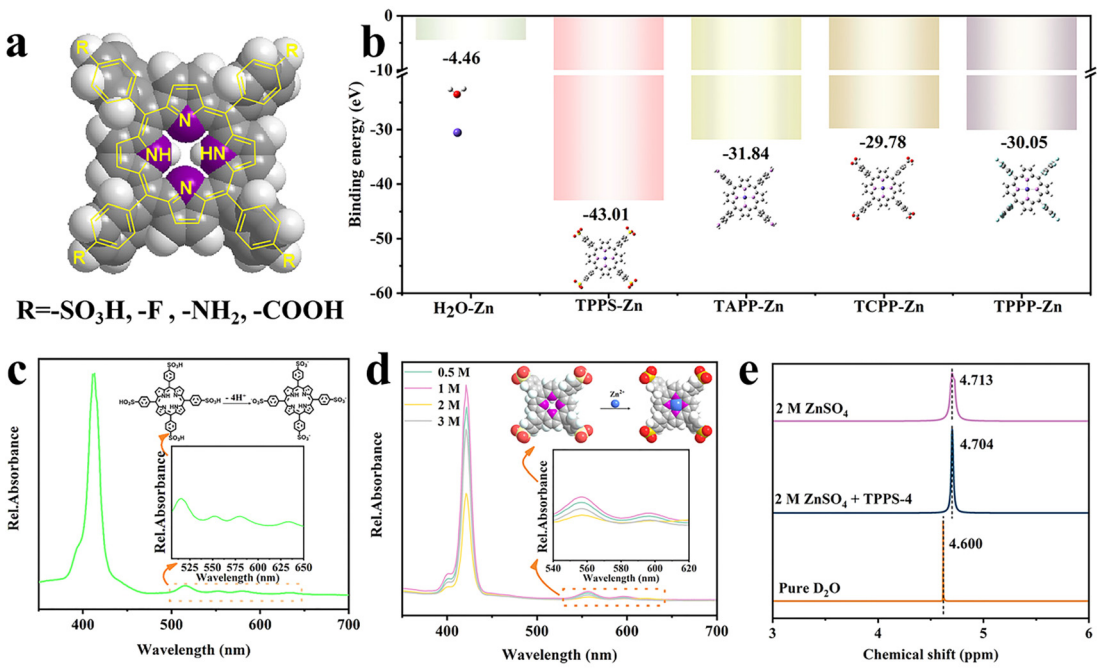

Fig. 1 (a) Molecular structure of different porphyrin additives. (b) Binding energies between Zn^{2+} with H_2O or internal cavities of different porphyrin additives. UV-vis absorption spectra of TPPS in (c) H_2O (insets: deprotonation pathway and structural evolution of TPPS) and (d) different concentrations of $ZnSO_4$ electrolytes (insets: molecular structure of $TPPS^{4-}$ internal cavity bound to Zn^{2+}). (e) ^1H NMR spectra of H_2O, 2 M $ZnSO_4$ + TPPS-4 and 2 M $ZnSO_4$.

Published on 17 December 2024. Downloaded on 25/11/2025 6:45:18 AM.

action of the interior and exterior features endows the possibility of trapping and transferring Zn^{2+}. Furthermore, the binding energies between Zn^{2+} and H_2O molecules, as well as the central cavity of different porphyrin additives (TPPS, TAPP, TCPP and TPPP), were explored by density functional theory (DFT) calculations. The interactions between Zn^{2+} and the central cavity of four porphyrin additives are higher than those between Zn^{2+} and H_2O, indicating that Zn^{2+} tends to bind to the central cavity of porphyrin additives more than H_2O (Fig. 1b). In addition to the central cavity, the peripheral substituents also show stronger binding ability with Zn^{2+} (Fig. S1†). By contrast, both the central cavity and the peripheral substituents of TPPS show the strongest combinations with Zn^{2+}, which endows TPPS with the best ability to reconstitute the solvation configurations of Zn^{2+}, that is, the Zn-porphyrin complex is formed to replace the hydrated $Zn(H_2O)_6^{2+}$, which could regulate Zn plating/stripping behaviors and prevent Zn corrosion. To further demonstrate the deprotonation pathway of TPPS and the interactions between Zn^{2+} and TPPS, UV-vis absorption spectroscopy was utilized. As illustrated in Fig. 1c, the absorption spectrum of TPPS presents a strong Soret band (S band) around 413 nm. In addition, there are four different weaker peaks (Q bands) around 635, 580, 552 and 515 nm, which are the typical peaks of porphyrin-free bases, indicating the existence of the deprotonated $TPPS^{4-}$.[41] After adding $ZnSO_4$ with different concentrations, the S band is observed at 421 nm, while the Q bands change significantly from four weaker peaks to two peaks at 558 nm and 597 nm (Fig. 1d), which coincides with the absorption peaks of Zn-TPPS, indicating the formation of the Zn-porphyrin complex even at very low $ZnSO_4$ concentrations.[42] This result is consistent with the strongest interaction between TPPS and Zn^{2+} from theoretical calculations. To further confirm the optimum concentration of TPPS in the $ZnSO_4$ electrolyte, Fourier transform infrared spectroscopy (FT-IR) was performed (Fig. S2†). In FT-IR spectra, the H–O stretching vibration at 3100–3400 cm^{-1} and the O═S═O/S–O bonds at 1020/1200 cm^{-1} red-shift after the addition of TPPS, indicating that the hydrogen bonding network of H_2O molecules was weakened due to the interaction between H_2O and TPPS. On the contrary, the H–O stretching vibration weakens when the concentration of TPPS exceeds 4 mg mL^{-1} (TPPS-4), suggesting the competition between larger concentrations of TPPS, which can also be observed from the digital photos of different electrolytes, wherein larger concentrations of TPPS were not completely soluble in the $ZnSO_4$ electrolyte (Fig. S3†). Therefore, it was concluded that the optimum concentration (TPPS-4) is conducive to the inhibition of hydrogen bonding, which is further verified by ^1H NMR spectra (Fig. 1e). From the ^1H NMR spectral results, the ^1H chemical shift of H_2O (4.600 ppm) shows an increasing trend with the addition of $ZnSO_4$ (4.713 ppm for 2 M $ZnSO_4$), indicating a strong coordination interaction between Zn^{2+} and H_2O, resulting in a decrease of the electron density around H_2O. However, when TPPS was added, the ^1H chemical shift of H_2O in 2 M $ZnSO_4$ gradually decreased from 4.713 ppm to 4.704 ppm, indicating that the TPPS additive can weaken the interaction between Zn^{2+} and H_2O, change the solvation structure of $Zn(H_2O)_6^{2+}$, and reduce the activity of free H_2O while being able to inhibit the corrosion reaction induced by H_2O.[43]

To further determine the optimal amount of the additive and discuss the difference between four peripheral substituents (–SO_3H, –COOH, –NH_2 and –F), long-term cycling stability in different electrolytes was performed using Zn||Zn symmetric cells. Firstly, at 0.5 mA cm^{-2}, Zn||Zn symmetric cells demonstrate longer cycling stability over 900 h and a smaller overpotential of 35.3 mV in 2 M $ZnSO_4$ + TPPS-4, which are superior to those of electrolytes without TPPS (57.0 mV, over 70 h), with TPPS-2 (90.8 mV, over 100 h), TPPS-6 (32.6 mV, over 790 h) and TPPS-8 (65.7 mV, over 380 h) (Fig. 2a and Fig. S4†). In addition, other electrolytes with TPPP (40.6 mV, over 400 h), TAPP (43.4 mV, over 350 h) and TCPP (30.7 mV, over 140 h) also show poor cycling stability and larger overpotential (Fig. S5 and S6†). The above results suggest that the electrolyte using 2 M $ZnSO_4$ + TPPS-4 is optimum. Even at 5 mA cm^{-2}, the Zn||Zn symmetric cells can also reposefully cycle over 800 h in 2 M $ZnSO_4$ + TPPS-4 (Fig. S7a†). Furthermore, the electrochemical reversibility of Zn||Zn symmetric cells in different electrolytes was also measured at different current densities (Fig. S7b†). In 2 M $ZnSO_4$ + TPPS-4, Zn||Zn symmetric cells demonstrate distinctly stable voltage hysteresis of 36.0, 38.4, 50.8 and 72.5 mV at 0.5, 1, 3 and 5 mA cm^{-2}, when the current density returns to 0.5 mA cm^{-2}, the overpotential approaches the initial state. Nevertheless, Zn||Zn symmetric cells in 2 M $ZnSO_4$ have the short-circuit phenomenon at 1 mA cm^{-2}, which proves the importance of the TPPS additive. In addition, the initial nucleation overpotential is also an irreplaceable indicator for measuring the electrochemical properties of different electrolytes.[30,31] Obviously, Zn||Zn symmetric cells in 2 M $ZnSO_4$ + TPPS-4 have a smaller initial nucleation overpotential (14.5 mV) than those of 2 M $ZnSO_4$, 2 M $ZnSO_4$ + TPPS-2/TPPS-6/TPPS-8 (53.0, 81.8, 23.0 and 64.5 mV, respectively), indicating that Zn^{2+} in 2 M $ZnSO_4$ + TPPS-4 can represent the lower energy nucleation barrier and the faster transfer and reaction kinetics compared with other electrolytes (Fig. 2b). Where after, the electrochemical nucleation and deposition behavior in different electrolytes can be compared with chronoamperometry (CA) curves (Fig. 2c). The 2D diffusion of abundant Zn^{2+} can generate irregular deposition products and increase the effective surface area, while the 3D nucleation process contributes to the formation of a dense and flat deposition layer.[34,38] The result shows that at a constant overpotential (−150 mV), the current density of the Zn anode gradually becomes stable at around 50 s (in 2 M $ZnSO_4$ + TPPS-4), while the Zn anode is difficult to stabilize beyond 200 s in 2 M $ZnSO_4$ electrolyte, implying that the TPPS additive can effectively restrict the irregular 2D diffusion of Zn^{2+} and enhance the electrochemical behavior of AZIBs. Afterwards, to explore the interfacial stability of Zn anodes in different electrolytes, electrochemical impedance spectroscopy (EIS) of the Zn||Zn symmetric cells was performed (Fig. 2d). It is obvious that Zn anode exhibits a smaller interfacial resistance value in 2 M

 This journal is © The Royal Society of Chemistry 2025

Published on 17 December 2024. Downloaded on 25/11/2025 6:45:18 AM.

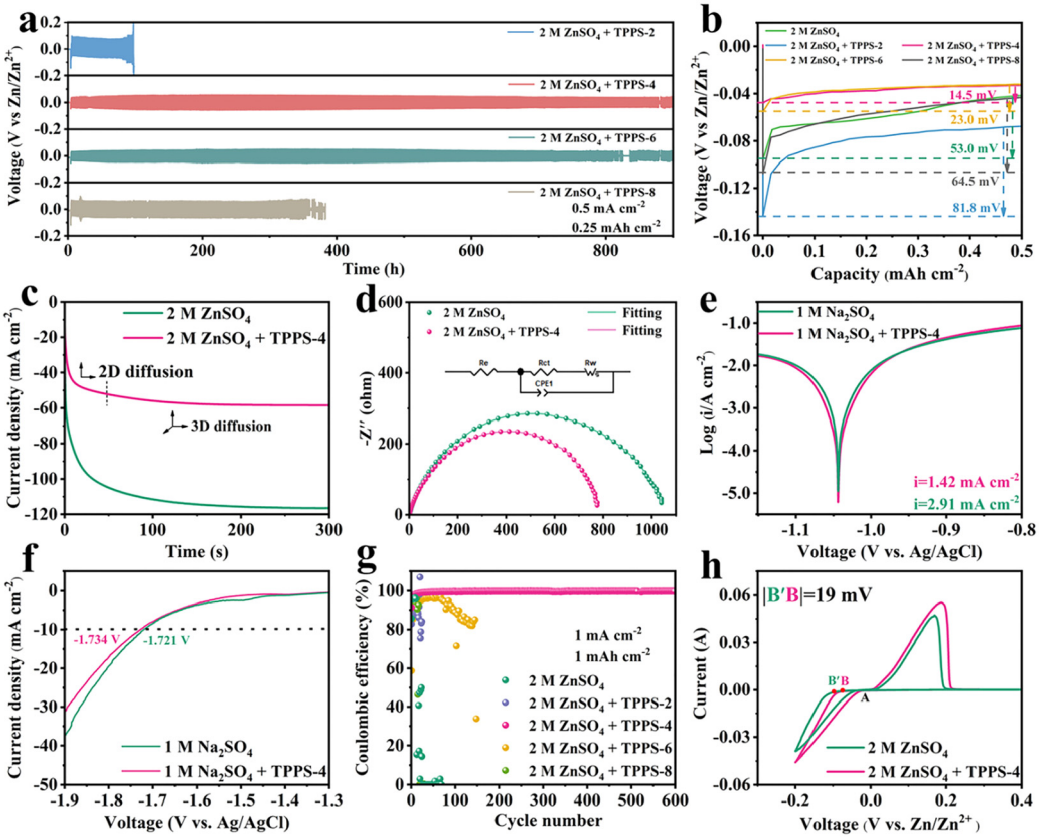

Fig. 2 (a) Long-term cycling performance of Zn||Zn symmetric cells in different electrolytes. (b) Nucleation overpotential at 0.5 mA cm^{-2} in different electrolytes. (c) CA curves and (d) Nyquist plots of Zn||Zn symmetric cells in 2 M $ZnSO_4$ and 2 M $ZnSO_4$ + TPPS-4. (e) Tafel plots and (f) LSV curves of Zn anode in 1 M Na_2SO_4 and 1 M Na_2SO_4 + TPPS-4. (g) CE and (h) CV curves of Zn||Cu asymmetric cells in different electrolytes.

$ZnSO_4$ + TPPS-4 (775 Ω) than 2 M $ZnSO_4$ (1040 Ω), which is due to the inhibition of corrosion reaction. Furthermore, after cycling 50 times, the interfacial resistance value of the Zn||Zn symmetric cells in 2 M $ZnSO_4$ + TPPS-4 decreases to 70.7 Ω, which may be caused by the facilitated charge transfer and the enhanced electrolyte-electrode interfacial wettability (Fig. S8†). The same phenomenon can also be recognized by the contact angle tests (Fig. S9†), where the contact angle of the electrolyte (2 M $ZnSO_4$ + TPPS-4, 68.3°) on the Zn surface is lower than that of the electrolyte (2 M $ZnSO_4$, 87.5°). It is concluded that the TPPS additive has stronger zincophilic properties than H_2O molecules, which not only reduce the activity of H_2O molecules but also improve the interfacial stability between the electrode and the electrolytes. Moreover, the corrosion resistance was further investigated by Tafel plots (Fig. 2e). The corrosion currents decreased from 2.91 (in 1 M Na_2SO_4) to 1.42 mA cm^{-2} (in 1 M Na_2SO_4 + TPPS-4). The lower corrosion current reflects that TPPS can effectively weaken the corrosion rate of Zn anodes. The linear scanning voltammetry (LSV) test can be used to investigate the HER kinetics.[30,31] The result demonstrates that 1 M Na_2SO_4 has a high initial potential of −1.721 V *vs.* Ag/AgCl, while the initial potential of 1 M Na_2SO_4 + TPPS-4 is −1.734 *vs.* Ag/AgCl (Fig. 2f). Therefore, the HER reaction was successfully suppressed after the addition of TPPS, which is beneficial to maintain a longer cycle life and the better electrochemical reversibility of AZOBs. Coulombic efficiency (CE) is engaged to measure the electrochemical reversibility and utilization of Zn. The Zn||Cu cells in 2 M $ZnSO_4$ + TPPS-4 can steadily cycle over 600 times, accompanied by a fascinating CE of 99.6%, which is significantly better than in other electrolytes (Fig. 2g). In addition, the voltage profiles display that the electrochemical reaction of Zn^{2+} on a Cu electrode in 2 M $ZnSO_4$ + TPPS-4 is more stable than in 2 M $ZnSO_4$ (Fig. S10†). To further investigate the nucleation kinetics, the cyclic voltammetry (CV) curves of Zn^{2+} deposited on Cu foils were analyzed (Fig. 2h). The potential difference between point A (at the intersection position) and points B/B′ was used to indicate the deposition overpotential of Zn^{2+}.[38,43] The overpotential in the Zn||Cu cells with 2 M $ZnSO_4$ + TPPS-4 decreases by about 18 mV compared with 2 M $ZnSO_4$, suggesting that TPPS can accelerate the nucleation kinetics and reduce the nucleation energy barrier of Zn^{2+}, and then TPPS can inhibit the formation of $Zn_4SO(OH)_6{\cdot}xH_2O$, improving the stability of the Zn anode.

The self-corrosion reaction is an important reference for measuring the stability of Zn anodes in different electrolytes.[44] X-ray diffraction (XRD) patterns show the self-corrosion of Zn foil, which is immersed in 2 M $ZnSO_4$ for 7 days. By contrast,

Published on 17 December 2024. Downloaded on 25/11/2025 6:45:18 AM.

there are no significant by-product diffraction peaks of the Zn foil in 2 M $ZnSO_4$ + TPPS-4, proving that the Zn-porphyrin complex can reduce the interaction between the Zn anode surface and H_2O molecules, further effectively inhibiting the corrosion reaction (Fig. S11†), and the result is consistent with the scanning electron microscope (SEM) images (Fig. S12†). Furthermore, the formation of nonconductive by-products $Zn_4SO(OH)_6{\cdot}xH_2O$ can be confirmed by XRD patterns (Fig. 3a). After the nucleation and deposition of Zn^{2+}, the apparent characteristic peak around 24.6° (in 2 M $ZnSO_4$) can be defined as that of $Zn_4SO(OH)_6{\cdot}xH_2O$.[38,43,44] However, in 2 M $ZnSO_4$ + TPPS-4, the intensity variation of $Zn_4SO(OH)_6{\cdot}xH_2O$ characteristic peak is negligible and the (001) plane diffraction peak gradually diminishes, suggesting that the introduction of TPPS can regulate the Zn metal planar orientation, and then the formation of the Zn-porphyrin complex can limit the parasitic reaction. Furthermore, SEM images were also investigated to observe the surface morphology of the Zn anode. Zn dendrites are numerous and grow unchecked as the number of cycles increases in 2 M $ZnSO_4$ (Fig. S13a and b†), while a symmetrical and compact Zn deposition layer was obtained during the deposition process in 2 M $ZnSO_4$ + TPPS-4 (Fig. S13c and

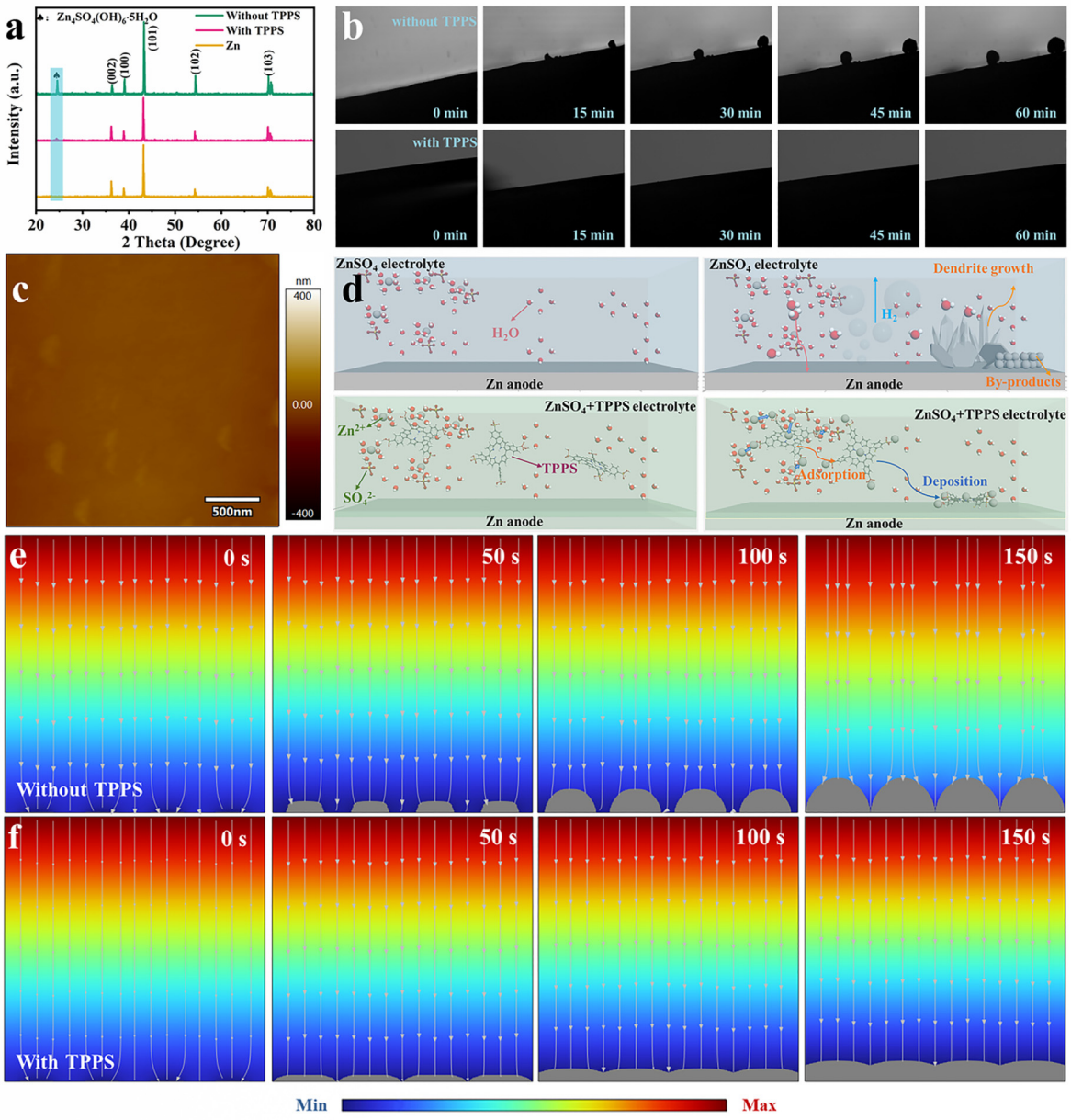

Fig. 3 (a) XRD patterns of Zn anodes after cycling in 2 M $ZnSO_4$ and 2 M $ZnSO_4$ + TPPS-4. (b) *In situ* optical microscope observations of the Zn deposition process in different electrolytes. (c) AFM image of Zn anodes in 2 M $ZnSO_4$ + TPPS-4. (d) Schematic of Zn deposition on different electrodes. Electric field distribution and the corresponding Zn^{2+} concentration field distribution on bare Zn in (e) 2 M $ZnSO_4$ and (f) 2 M $ZnSO_4$ + TPPS-4.

This journal is © The Royal Society of Chemistry 2025

Published on 17 December 2024. Downloaded on 25/11/2025 6:45:18 AM.

d†). Cross-section SEM images also demonstrate that the addition of TPPS and the formation of the Zn-porphyrin complex can obviously improve the collapse phenomenon of the Zn anode surface (Fig. S14†). Meanwhile, *in situ* optical microscopy was employed to understand further the Zn deposition process and the formation of $Zn_4SO(OH)_6{\cdot}xH_2O$. The dendrites produced by Zn deposition appear within 15 min and continue to grow on the Zn anode surface, while the introduction of the TPPS additive generates the planar nucleation and dendrite-free Zn deposition; thus, the short-circuit phenomenon was significantly inhibited in 2 M $ZnSO_4$ + TPPS-4 (Fig. 3b). Furthermore, atomic force microscopy (AFM) images also demonstrate that the Zn anode surface is smooth and uniform after plating/stripping 100 times in 2 M $ZnSO_4$ + TPPS-4 (Fig. 3c), thereby resulting in a positive impact of the Zn plating/stripping and decreasing the formation of nonconductive by-products. By contrast, in 2 M $ZnSO_4$, $Zn_4SO(OH)_6{\cdot}xH_2O$ and Zn deposition grow along the convex surface, especially in the vertical direction as protuberances (Fig. S15†), which is consistent with the SEM and *in situ* optical microscopy results.[45] Therefore, the addition of TPPS can promote the uniform distribution of Zn^{2+} and avoid the accumulation of protrusions and dendrites (Fig. 3d), contributing to the reduction of HER. The interesting phenomenon is also confirmed by finite element simulations using COMSOL multiphysics. In 2 M $ZnSO_4$, the asymmetrical and intensive electric field distribution is caused by the surface protrusions of the Zn anode. Then, the electric field density at the protrusion gradually increases with the prolonged deposition time, which can give rise to the phenomenon of Zn preferentially deposited on the surface protrusions of the Zn anode, and the uncontrollable protruding dendrite can puncture fiberglass, causing irreversible damage to batteries (Fig. 3e).[12] By contrast, with the increase in deposition time, the change in electric field distribution around Zn protrusions in 2 M $ZnSO_4$ + TPPS-4 is approximately negligible, and then the generation of protrusions is alleviated, demonstrating the more uniform Zn^{2+} deposition (Fig. 3f), which displays the promising TPPS additive for enhancing the electrochemical performance of Zn anodes.[12]

To more intuitively explore the mechanism of TPPS additive in 2 M $ZnSO_4$ electrolyte, molecular dynamics (MD) simulations were performed (Fig. 4a and b). The combination of TPPS and $ZnSO_4$ is simulated and demonstrated as radial distribution functions (RDFs) and coordination numbers (CNs).[12,36,39] Obviously, the correlation between Zn^{2+} and TPPS can be observed from the TPPS molecule peaks at 5.5 and 7.5 Å (Fig. S16a†), which is also confirmed by the smaller TPPS molecule peak and the higher CNs of SO_3^{2-}-Zn^{2+} than those of SO_3^{2-}-SO_4^{2-} (Fig. S16b†). Furthermore, the TPPS additive can effectively inhibit the coordination of Zn^{2+} and SO_4^{2-}, thus improving the utilization rate of Zn^{2+} and restraining the production of nonconductive by-products (Fig. 4c). Therefore, the TPPS additive can break the Zn^{2+} solvation sheath and facilitate the Zn^{2+} transportation. Subsequently, to further investigate the inhibition of hydrogen evolution reaction by TPPS

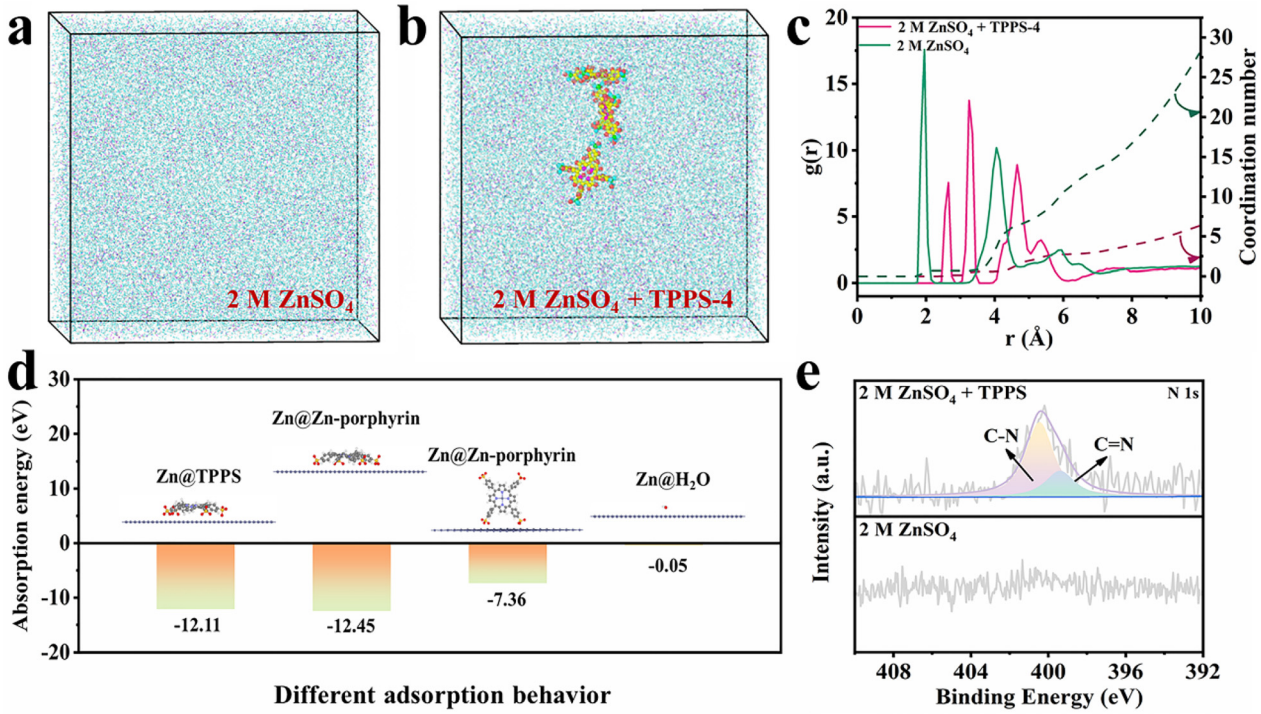

Fig. 4 3D snapshots of (a) 2 M $ZnSO_4$ and (b) 2 M $ZnSO_4$ + TPPS-4 electrolytes from MD simulations. (c) RDFs of Zn^{2+}-SO_4^{2-} in different electrolytes. (d) Absorption energy comparison of TPPS, Zn-porphyrin complex and H_2O on Zn crystal planes. (e) N 1s XPS spectra of the Zn anode after cycling in 2 M $ZnSO_4$ and 2 M $ZnSO_4$ + TPPS-4.

Published on 17 December 2024. Downloaded on 25/11/2025 6:45:18 AM.

additive, the hydrogen adsorption Gibbs free energy (ΔG_H) was also calculated (Fig. S17†). It is widely known that the ΔG_H value approaches 0, which can lead to the hydrogen evolution reaction. Among them, TPPS exhibits a smaller ΔG_H value (−6.49 eV) than Zn (−3.78 eV), indicating that the TPPS additive is beneficial in inhibiting the HER. To further explore the function of the Zn-porphyrin complex, the absorption energy corresponding to different absorption behaviors was calculated (Fig. 4d).[12] The result shows that TPPS, Zn-porphyrin complex and H_2O on Zn crystal planes demonstrate negative adsorption energy, indicating the spontaneity of different absorption behaviors. Among them, the Zn-porphyrin complex has lower adsorption energy and paramount absorption behavior, which is parallel to the Zn crystal planes. Therefore, the Zn-porphyrin complex can serve as a protective layer to prevent the unrestrained growth of Zn dendrites, which can effectively prevent short-circuiting and improve the electrochemical performance. To further confirm the advantageous phenomenon of Zn@Zn-porphyrin, several characterization tests of the Zn anode after cycling in different electrolytes were provided. Firstly, X-ray photoelectron spectroscopy (XPS) certifies the valence states of different elements. In the N 1s spectra, two different single peaks can be observed at 399.5 and 400.5 eV (C═N and C–N bond, respectively) on the Zn anode in 2 M $ZnSO_4$ + TPPS-4 (Fig. 4e), which is obviously different from 2 M $ZnSO_4$. The existence of TPPS can also be confirmed by $S^{(2/3)}O_3^-$ and $S^{(1/3)}O_3^-$ in S 2p spectra (Fig. S18a†).[39] Furthermore, in the O 1s spectra, the characteristic peak intensity of $ZnO/Zn(OH)_2$ decreases obviously in 2 M $ZnSO_4$ + TPPS-4, indicating that the production of nonconductive by-products is controlled (Fig. S18b†). Secondly, the energy-dispersive spectroscopy (EDS) elemental mapping images of the Zn anode in 2 M $ZnSO_4$ + TPPS-4 also show the uniform distribution of Zn, N, O and S elements (Fig. S19†), confirming the existence of TPPS on the Zn anode surface. However, in 2 M $ZnSO_4$, with the formation of $Zn_4SO(OH)_6{\cdot}xH_2O$, the content of O and S elements increases significantly (Fig. S20†), which is consistent well with the XPS result. Therefore, TPPS displays a strong combination with Zn^{2+}, and then the generated Zn-porphyrin complex can replace the hydrated $Zn(H_2O)_6^{2+}$, which could regulate Zn plating/stripping behaviors and prevent Zn corrosion.

To further research the practical application capability of the TPPS additive, the full cell was assembled with a QAP

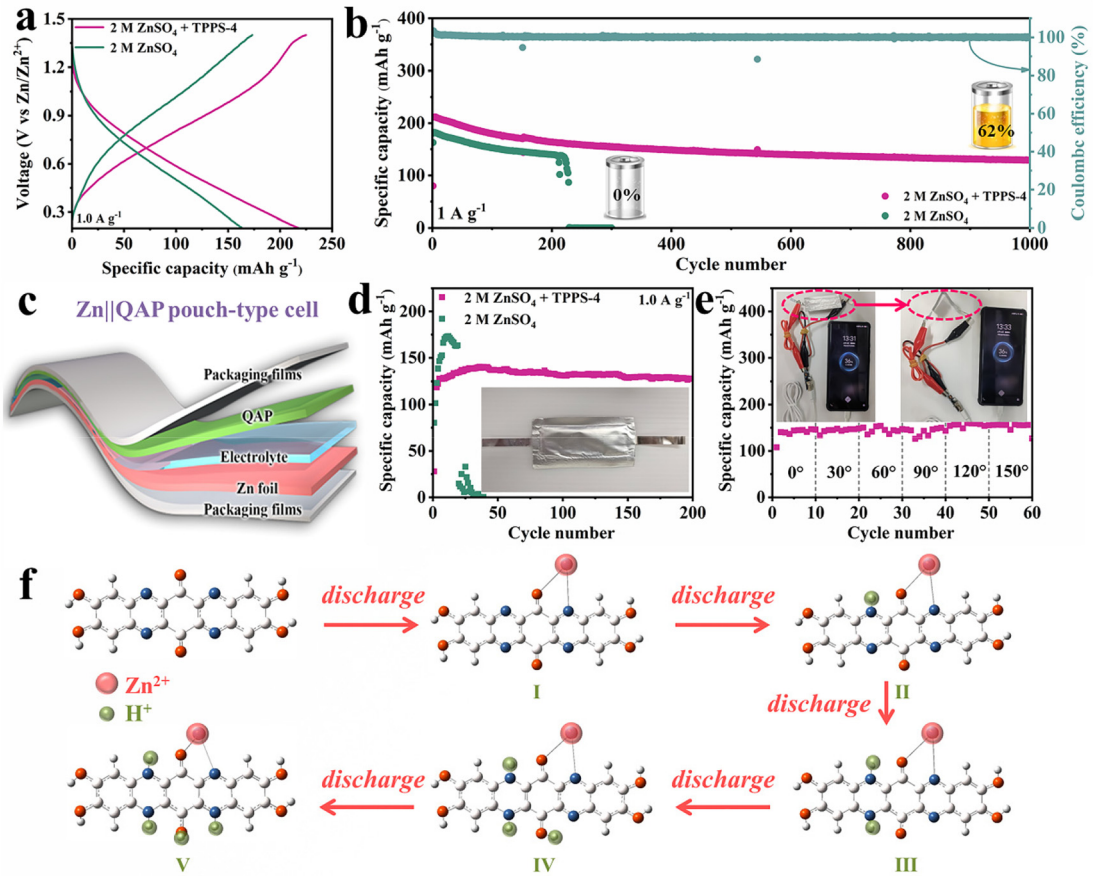

Fig. 5 (a) GCD profiles and (b) long-term cycling stability of the Zn||QAP full cell at 1.0 A g^{-1}. (c) Schematic configuration of the Zn||QAP pouch-type cell. (d) Long-term cycling stability of the Zn||QAP pouch-type cell at 1.0 A g^{-1} (the inset is Zn||QAP pouch-type cell). (e) Bending test for the Zn||QAP pouch-type cell at 1.0 A g^{-1} (the inset is the Zn||QAP pouch-type cell powering a smartphone). (f) Most stable structure of the QAP repetitive unit at each discharge stage.

 This journal is © The Royal Society of Chemistry 2025

Published on 17 December 2024. Downloaded on 25/11/2025 6:45:18 AM.

cathode, Zn anode and different electrolytes. The synthetic details of QAP are presented in the ESI (Schemes S1, S2 and Fig. S21†). In CV curves, the approximate oxidation/reduction peak values of the Zn‖QAP full cell with different electrolytes demonstrate that the addition of TPPS did not change the redox mechanism of QAP (Fig. S22†). However, the GCD profiles of the Zn‖QAP full cell with TPPS display a higher reversible specific capacity (Fig. 5a), demonstrating excellent Zn^{2+} utilization. Furthermore, the Zn‖QAP full cell with TPPS can also maintain a low-capacity loss of 0.038% per cycle with a high coulombic efficiency of ~100% at 1.0 A g^{-1} (Fig. 5b), while the Zn‖QAP full cell without TPPS has a short-circuit phenomenon after cycling 200 times. Notably, the Zn‖QAP full cell also displays a superior rate capability in 2 M $ZnSO_4$ + TPPS-4, and then the specific capacities can reach 206.2, 160.2, 145.7, 137.4, 130.9, 119.5 and 103.5 mA h g^{-1} when the current densities are 0.2, 0.4, 0.6, 0.8, 1.0, 2.0 and 5.0 A g^{-1}, respectively (Fig. S23a†). After cycling 80 times, the specific capacity can be retained to 150.0 mA h g^{-1} at 0.2 A g^{-1}, while the Zn‖QAP full cell in 2 M $ZnSO_4$ is short-circuited (Fig. S23b†). Furthermore, EIS tests were also conducted before and after 10 and 60 cycles for the Zn‖QAP full cell (Fig. S24†). Clearly, the values decrease gradually from 69.5 to 14.5 and 10.9 Ω, indicating the rapid and stable reaction kinetics. Subsequently, to further discuss the practical application, the electrochemical behavior of the Zn‖QAP full cell was also tested at −10 °C. The result shows that the Zn‖QAP full cell has a high reversible specific capacity of 215.3 mA h g^{-1} at 0.05 A g^{-1} (Fig. S25a†) and a stable long-cycle capability at 0.5 A g^{-1} (Fig. S25b†). Meanwhile, for a more in-depth understanding of the practical application of TPPS additive, a Zn‖QAP pouch-type cell was fabricated (Fig. 5c). Among them, the Zn‖QAP pouch-type cell can also exhibit excellent long-term cycling stability at 1.0 A g^{-1} (Fig. 5d). Even at different bending angles, the change in specific capacities is negligible (Fig. 5e), which can charge a smartphone using the booster module (the illustration of Fig. 5e). Therefore, TPPS can effectually inhibit the arbitrary growth of Zn dendrites and decrease the side reactions, improving the electrochemical performance. To investigate the ion storage mechanism of QAP in detail, some comparative experiments were performed. Firstly, CV curves demonstrate that the QAP cathode has a larger integration area in 2 M $ZnSO_4$ + TPPS than in H_2SO_4 + TPPS (pH = 4.8), while the overlapping area is defined as the co-existence mechanism (Fig. S26†).[16] Secondly, the reversible specific capacities of QAP in 2 M $Zn(CF_3SO_3)_2$/ACN + TPPS and H_2SO_4 + TPPS are about 100 and 200 mA h g^{-1}, respectively (Fig. S27†), which is equal to that of 2 M $ZnSO_4$ + TPPS (Fig. S28†). Therefore, QAP demonstrates the H^+ and Zn^{2+} co-storage mechanism, and then the proportion of H^+ and Zn^{2+} is 1 : 2, which is consistent with the inductively coupled plasma atomic emission spectroscopy (ICP-AES) result (Zn^{2+} = 37.45%, H^+ = 62.55%). The addition of TPPS promotes the storage of both H^+ and Zn^{2+}, further confirming the H^+ and Zn^{2+} co-storage mechanism of QAP. To further explore the H^+ and Zn^{2+} co-storage mechanism and the optimal structure mode, the binding energies at different states were provided (Fig. S29–S32†). Among them, the lowest binding energies are for the optimized structure.[16,39,46] Therefore, the QAP repeating unit can accept 1 Zn^{2+} and 1 H^+ at the oxygen side, and then the other side can interact with the other 3 H^+ (Fig. 5f). The calculated result demonstrates the redox reactions are spontaneous and sequential, realizing the H^+ and Zn^{2+} co-storage mechanism.

Conclusions

In this work, we showcase the fascinating macromolecular electrolyte engineering to tune the Zn-ion solvation chemistry and boost H^+ storage toward stable AZOBs. Screening a series of porphyrin additives indicates that TPPS can effectively inhibit the common side reactions and enhance the electrochemical performance. The combined spectral characterizations, DFT computations, and MD/COMSOL simulations unveil that TPPS, which features a zincophilic central cavity and deprotonation-capability and peripheral $-SO_3H$ to generate the Zn-porphyrin complex, could break the Zn^{2+} solvation sheath, facilitate the Zn^{2+} transportation and uniform deposition, and inhibit the occurrence of HER and the formation of nonconductive by-products $Zn_4SO(OH)_6{\cdot}xH_2O$. Furthermore, the full cell and the pouch-type cell were assembled by coupling the QAP cathode with the optimum electrolyte, which harvests the improved specific capacity in view that the dissociation of H^+ from the TPPS additive could boost H^+ storage of the QAP cathode and achieve the long-term cycling stability with a low-capacity loss of 0.038% per cycle after 1000 cycles at 1.0 A g^{-1}. This research indicates an irreplaceable direction for accelerating the commercialization process of AZOBs and provides original thinking for the application of porphyrin additives in practice.

Author contributions

L. C., M. L. and X. Z. contributed equally to this work. The manuscript was written with contributions from all authors. All authors have given approval to the final version of the manuscript. L. C., M. L. and X. Z.: investigation and data curation, W. W.: formal analysis validation. X. Z.: theoretical calculation. H. G. W. and L. Z.: conceptualization, supervision, writing–review and editing, and funding acquisition.

Data availability

All experimental data supporting the procedures are available in the ESI.†

Conflicts of interest

There are no conflicts to declare.

Published on 17 December 2024. Downloaded on 25/11/2025 6:45:18 AM.

Acknowledgements

This work is financially supported by the National Natural Science Foundation of China (Grant No. 52172186) and the Science & Technology Department of Jilin Province (No. 20230508057RC).

References

1 W. Sun, F. Wang, B. Zhang, M. Zhang, V. Küpers, X. Ji, C. Theile, P. Bieker, K. Xu, C. Wang and M. Winter, *Science*, 2021, **371**, 46.
2 S. W. D. Gourley, R. Brown, B. D. Adams and D. Higgins, *Joule*, 2023, **7**, 1415.
3 W. Sun, F. Wang, S. Hou, C. Yang, X. Fan, Z. Ma, T. Gao, F. Han, R. Hu, M. Zhu and C. Wang, *J. Am. Chem. Soc.*, 2017, **139**, 9775.
4 F. Wan and Z. Niu, *Angew. Chem., Int. Ed.*, 2019, **58**, 16358.
5 D. Lin and Y. Li, *Adv. Mater.*, 2022, **34**, 2108856.
6 Z. Li, J. Tan, Y. Wang, C. Gao, Y. Wang, M. Ye and J. Shen, *Energy Environ. Sci.*, 2023, **16**, 2398.
7 A. Zhang, R. Zhao, Y. Wang, J. Yue, J. Yang, X. Wang, C. Wu and Y. Bai, *Angew. Chem., Int. Ed.*, 2023, **62**, e202313163.
8 Y. Lv, Y. Xiao, L. Ma, C. Zhi and S. Chen, *Adv. Mater.*, 2022, **34**, 2106409.
9 M. Shi, B. Wang, Y. Shen, J. Jiang, W. Zhu, Y. Su, M. Narayanasamy, S. Angaiah, C. Yan and Q. Peng, *Chem. Eng. J.*, 2020, **399**, 125627.
10 J. Yang, B. Yin, S. Zhang, Y. Sun, J. Li, D. Su and T. Ma, *Small*, 2023, **19**, 2304913.
11 Q. Q. Sun, T. Sun, J. Y. Du, Z. L. Xie, D. Y. Yang, G. Huang, H. M. Xie and X. B. Zhang, *Angew. Chem., Int. Ed.*, 2023, **62**, e202307365.
12 J. Wang, X. Zhang, Z. Liu, J. Yu, H. G. Wang, X. L. Wu, F. Cui and G. Zhu, *Angew. Chem., Int. Ed.*, 2024, **63**, e202401559.
13 K. W. Nam, S. S. Park, R. D. Reis, V. P. Dravid, H. Kim, C. A. Mirkin and J. F. Stoddart, *Nat. Commun.*, 2019, **10**, 4948.
14 W. Li, H. Xu, H. Zhang, F. Wei, L. Huang, S. Ke, J. Fu, C. Jing, J. Cheng and S. Liu, *Nat. Commun.*, 2023, **14**, 5235.
15 J. Liu, Y. Zhou, G. Xing, M. Qi, Z. Tang, O. Terasaki and L. Chen, *Adv. Funct. Mater.*, 2024, **34**, 2312636.
16 J. Chu, Z. Liu, J. Yu, L. Cheng, H. G. Wang, F. Cui and G. Zhu, *Angew. Chem., Int. Ed.*, 2024, **63**, e202314411.
17 L. Zhong, C. Wang, J. He, Z. Lin, X. Yang, R. Li, S. Zhan, L. Zhao, D. Wu, H. Chen, Z. Tang, C. Zhi and H. Lv, *Adv. Mater.*, 2024, **36**, 2314050.
18 S. Niu, Y. Wang, J. Zhang, Y. Wang, Y. Tian, N. Ju, H. Wang, S. Zhao, X. Zhang, W. Zhang, C. Li and H. B. Sun, *Small*, 2024, **20**, 2309022.
19 Z. Lin, H. Y. Shi, L. Lin, X. Yang, W. Wu and X. Sun, *Nat. Commun.*, 2021, **12**, 4424.
20 Y. Chen, J. Li, Q. Zhu, K. Fan, Y. Cao, G. Zhang, C. Zhang, Y. Gao, J. Zou, T. Zhai and C. Wang, *Angew. Chem., Int. Ed.*, 2022, **61**, e202116289.
21 Y. Gao, G. Li, F. Wang, J. Chu, P. Yu, B. Wang, H. Zhan and Z. Song, *Energy Storage Mater.*, 2021, **40**, 31–40.
22 Z. Song, L. Miao, H. Duan, Y. Lv, L. Gan and M. Liu, *Angew. Chem., Int. Ed.*, 2024, **63**, e202401049.
23 Z. Yi, G. Chen, F. Hou, L. Wang and J. Liang, *Adv. Energy Mater.*, 2021, **11**, 2003065.
24 J. Chen, W. Zhao, J. Jiang, X. Zhao, S. Zheng, Z. Pan and X. Yang, *Energy Storage Mater.*, 2023, **59**, 102767.
25 L. Hong, L. Y. Wang, Y. Wang, X. Wu, W. Huang, Y. Zhou, K. X. Wang and J. S. Chen, *Adv. Sci.*, 2022, **9**, 2104866.
26 J. Cao, D. Zhang, X. Zhang, Z. Zeng, J. Qin and Y. Huang, *Energy Environ. Sci.*, 2022, **15**, 499.
27 H. Cui, J. Zhu, R. Zhang, S. Yang, C. Li, Y. Wang, Y. Hou, Q. Li, G. Liang and C. Zhi, *J. Am. Chem. Soc.*, 2024, **146**, 15393–15402.
28 W. Du, J. Yan, C. Cao and C. C. Li, *Energy Storage Mater.*, 2022, **52**, 329–354.
29 H. Peng, X. Wang, F. Yang, Z. Liu, H. Lei, S. Cui, X. Xie and G. Ma, *Chem. Eng. J.*, 2023, **474**, 145864.
30 X. Yang, Q. Zhou, S. Wei, X. Guo, P. J. Chimtali, W. Xu, S. Chen, Y. Cao, P. Zhang, K. Zhu, H. Shou, Y. Wang, X. Wu, C. Wang and L. Song, *Small Methods*, 2024, **8**, 2301115.
31 K. Zhao, G. Fan, J. Liu, F. Liu, J. Li, X. Zhou, Y. Ni, M. Yu, Y. M. Zhang, H. Su, Q. Liu and F. Cheng, *J. Am. Chem. Soc.*, 2022, **144**, 11129–11137.
32 J. Yin, M. Li, X. Feng, T. Cui, J. Chen, F. Li, M. Wang, Y. Cheng, S. Ding, X. Xu and J. Wang, *J. Mater. Chem. A*, 2024, **12**, 1543.
33 T. C. Li, Y. V. Lim, X. L. Li, S. Luo, C. Lin, D. Fang, S. Xia, Y. Wang and H. Y. Yang, *Adv. Energy Mater.*, 2022, **12**, 2103231.
34 Y. Su, X. Wang, M. Zhang, H. Guo, H. Sun, G. Huang, D. Liu and G. Zhu, *Angew. Chem., Int. Ed.*, 2023, **62**, e202308182.
35 G. Zhang, L. Fu, Y. Chen, K. Fan, C. Zhang, H. Dai, L. Guan, M. Mao, J. Ma and C. Wang, *Adv. Mater.*, 2024, **36**, 2405949.
36 K. Zhao, G. Fan, J. Liu, F. Liu, J. Li, X. Zhou, Y. Ni, M. Yu, Y. M. Zhang, H. Su, Q. Liu and F. Cheng, *J. Am. Chem. Soc.*, 2022, **144**, 11129.
37 L. Miao, R. Wang, W. Xin, L. Zhang, Y. Geng, H. Peng, Z. Yan, D. Jiang, Z. Qian and Z. Zhu, *Energy Storage Mater.*, 2022, **49**, 445.
38 X. Zhang, Y. Liu, P. Shen, L. Ren, D. Han, M. Feng and H. G. Wang, *Adv. Funct. Mater.*, 2024, **34**, 2400032.
39 L. Cheng, L. Chen, J. Yu, L. Zhao, W. Wang, Z. Yang and H. G. Wang, *J. Colloid Interface Sci.*, 2024, **663**, 656.
40 H. G. Wang, Q. Wu, L. Cheng, L. Chen, M. Li and G. Zhu, *Energy Storage Mater.*, 2022, **52**, 495–513.
41 D. L. Akins, H. R. Zhu and C. Guo, *J. Phys. Chem.*, 1994, **98**, 3612.
42 W. M. Hikal and H. J. Harmon, *Polyhedron*, 2009, **28**, 113.

 This journal is © The Royal Society of Chemistry 2025

43 H. Qin, W. Kuang, N. Hu, X. Zhong, D. Huang, F. Shen, Z. Wei, Y. Huang, J. Xu and H. He, *Adv. Funct. Mater.*, 2022, **32**, 2206695.
44 Y. Li, H. Jia, U. Ali, B. Liu, Y. Gao, L. Li, L. Zhang, F. Chai and C. Wang, *Chem. Eng. J.*, 2022, **450**, 138374.
45 Y. Guo, C. Luo, M. Yang, H. Wang, W. Ma, K. Hu, L. Li, F. Wu and R. Chen, *Angew. Chem., Int. Ed.*, 2024, **63**, e202406597.
46 L. Cheng, J. Yu, L. Chen, J. Chu, J. Wang, H. G. Wang, D. Feng, F. Cui and G. Zhu, *Small*, 2023, **19**, 2301578.

Published on 17 December 2024. Downloaded on 25/11/2025 6:45:18 AM.